IEEE Access
Multidisciplinary | Rapid Review | Open Access Journal

Received December 29, 2021, accepted February 5, 2022, date of publication February 14, 2022, date of current version February 24, 2022.

Digital Object Identifier 10.1109/ACCESS.2022.3151470

Design and Characterization of Magnetic Scaffolds for Bone Tumor Hyperthermia

MATTEO BRUNO LODI[1,2], (Student Member, IEEE), ANTONIS MAKRIDIS[3], NICOLA M. CARBONI[4], KONSTANTINA KAZELI[3], NICOLA CURRELI[5], THEODOROS SAMARAS[3], (Member, IEEE), MAKIS ANGELAKERIS[3], GIUSEPPE MAZZARELLA[1,2], (Senior Member, IEEE), AND ALESSANDRO FANTI[1,2], (Member, IEEE)

[1]Department of Electrical and Electronic Engineering, University of Cagliari, 09123 Cagliari, Italy
[2]Inter-University National Research Center on Interactions Between Electromagnetic Fields and Biosystems, 16145 Genova, Italy
[3]Magnetic Nanostructure Characterization: Technology and Applications, CIRI-AUTH, 57001 Thessaloniki, Greece
[4]Department of Mathematics and Informatics, University of Cagliari, 09123 Cagliari, Italy
[5]Istituto Italiano di Tecnologia, 16163 Genoa, Italy

Corresponding author: Alessandro Fanti (alessandro.fanti@unica.it)

ABSTRACT Magnetic tissue scaffolds are a promising powerful tool for performing interstitial tumor hyperthermia against the residual bone cancer cells, after surgical intervention. The design of the implant architecture is crucial for several biomedical requirements. However, to date, the influence of implant topology on the hyperthermia treatment outcome has never been assessed. Furthermore, the heating ability is a function of sample mass and geometry. In this work, a simple methodology for designing biomimetic scaffolds using triply periodic minimal surfaces is presented. A set of geometries is 3D printed by fused deposition modeling, using a commercial poly-lactic acid filament filled with magnetite particles, never tested for biomedical applications. Magnetic scaffolds were thoroughly characterized by performing static magnetic measurements, differential scanning calorimetric and thermogravimetric analysis, but, mostly, by carrying out calorimetric measurements to determine their hyperthermic potential under different experimental conditions. Numerical multiphysics simulations with a commercial finite element software were performed, resulting in good agreement with the measurements. The scaffolds were exposed to a magnetic field with 15 mT strength, working at 400 kHz, in air, and the surface temperature was recorder using infrared camera. The manufactured magnetic scaffolds can increase the temperature above 41°C (about 54-57°C), in 40-60 s. In distilled water, for a 30 mT magnetic field and 400 kHz, the temperature was recorded using an optic fiber and we observed that all the sample could be used as thermo-seed for cancer therapy. Finally, the scaffolds were tested in agarose phantoms and their hyperthermic potential was quantified.

INDEX TERMS Biomagnetics, computational geometry, hyperthermia, magnetic scaffolds, radiofrequency heating, triply periodical minimal surface.

I. INTRODUCTION

AGNETO-responsive biomaterials are multifunctional devices which can be synthesized by chemical doping of bioceramics with ferrous ions [1]–[3] or by loading polymers with micro- or nanoparticles [4]–[6] (Fig. 1). The possibility to produce a magnetic implant, or tissue scaffold (MagS), has drawn the attention of materials scientists, biomedical engineer and clinicians for developing active, controllable devices for several biomedical applications, especially related to bone tissue and orthopedic [7]–[12]. Indeed, by remotely controlling the implanted magnetic biomaterial with electromagnetic fields it is possible to achieve unexpected theranostic performances with a single versatile platform. For instance, by using low-frequency magnetic fields, the mechano-transduction and healing control was demonstrated for bone tissue engineering, by controlling local Ca^{2+} fluxes and acting on integrins expression [12]–[14]. Furthermore, static magnetic field can be used for controlling cell patterning of complex 3D bio-structures [15]. Again, with the same magnetic scaffold is also possible to non-invasively monitor the tissue growth by using magnetic resonance

The associate editor coordinating the review of this manuscript and approving it for publication was Rajeswari Sundararajan.

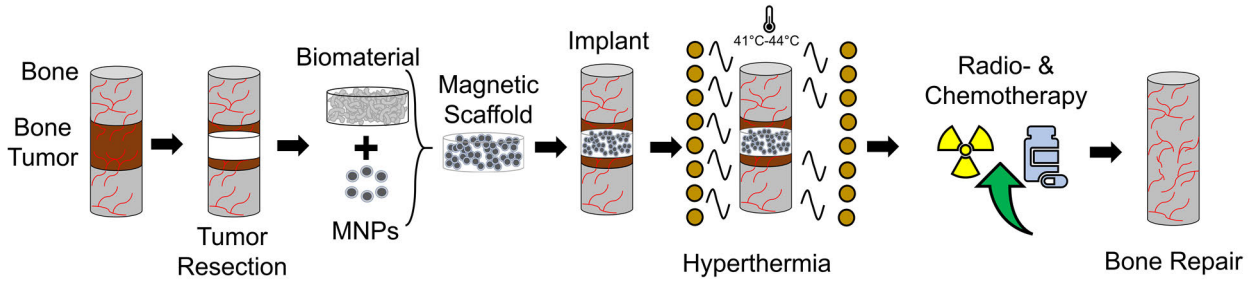

FIGURE 1. Rationale of the interstitial hyperthermia treatment using magnetic prosthetic implants, namely magnetic scaffolds composed of biomaterials and magnetic particles.

imaging (MRI), quantifying the changes in the relaxation times of the nanocomposite implant [16]–[18]. Furthermore, this class of third generation biomaterials, if exposed to a radiofrequency field, dissipate noticeable heat, which can be used to trigger the drug release of chemotherapeutics [1], [6].

In this framework, considering the osteogenic features, the tissue engineering potential and the possibility to be used as local heaters, MagS are currently under investigation as a complete tool for orthopedic oncology, as shown in Fig. 1. Primary and secondary bone tumors are incapacitating, painful and potentially lethal pathologies [19]. Among malignant bone neoplasms, osteosarcomas are chemo- and radio-resistant aggressive tumors, for which 60% survival rate and 40% recurrence rate are reported [20], [21]. Orthopaedic oncology is a clinical field constantly seeking patient-specific therapies to lower the recurrence rate of bone neoplasms, increase the survival rate and improving the quality of live [19]–[21]. Currently, the gold-standard treatment strategy of bone cancers is the systemic chemotherapy, followed by surgery, i.e., curettages, osteotomies, limb sparing [21]. However, the surgical approach results in disabling outcomes and disabilities, which call for a graft, i.e., a scaffold able to improve bone healing [22], [23]. This implant must be used since it has the role of fulfilling the bone defect and withstand the bone healing process. Moreover, given the unclear tumor margins, after the intervention chemo/radio-resistant neoplastic cells could remain on site residual. Therefore, a strategy for local intervention is required to clear the surgical field from residual cancerous cells, and then with the goal to improve bone healing, in the post-operative phase, as sketched in Fig. 1. MagS can carry out these tasks.

Indeed, to date, the alternative therapeutic approaches (e.g., embolization, cryotherapy) under investigation demonstrated a scarce translation potential [19]–[21]. So, electromagnetic (EM) biophysical therapies stood out as attractive, effective and less invasive treatment strategies [21]. In particular, the hyperthermia treatment (HT) of bone tumors performed, after surgical resection, by using MagS as local, interstitial heaters and biocompatible thermo-seeds exposed to a RF magnetic field is forecast to become a promising therapeutic strategy in orthopaedic oncology [1], [3], [11], [24], [25]. HT is a thermal therapy which aims to raise the tissue temperature in the range 41-45°C for 30-60 min in order to elicit the immune system response, increase cytotoxicity, while increasing the permeability to chemotherapeutic drugs and enhancing the radiation effectiveness [26], [27]. HT is known to stimulate locally the bone growth by initiating a signaling cascade and activating osteogenic growth factors [28]–[32]. Therefore, the destruction of the tumor followed by the increased deposition of healthy bone guided by a biomaterial is a rather appealing and favorable condition for clinical practice (Fig. 1).

To fully exploit the potential of magnetic-responsive and multifunctional biomaterials for planning and performing a possibly optimal interstitial hyperthermia treatment, followed by an excellent bone repair and healing, the design of the biomaterial must be carried out in a novel and interdisciplinary perspective. Despite the plethora of available MagS [1]–[18], [24], [25], the research efforts were mainly oriented towards the investigation of the material synthesis issues [33], as in the case of PVDF embedding CoFe2O4 scaffolds with woven interconnected structure developed using the solvent casting method [34], or toward the proof-of-concept of heating capability when exposed to a RF magnetic field, such as the case of the 90°-sfiber mesh 3D printed poly-caprolactone (PCL) scaffold loaded with magnetic hydroxyapatite particles [35]. As a matter of fact, in the open literature, it is difficult to find a study about MagS which combines the orthopaedic requirements while carrying out a through and extensive characterization of the hyperthermic potential, while accounting for the influence of the geometrical features.

In clinical practice, the implanted biomaterials are required to have a porous (70-90%) interconnected structure, with biomimetic properties, i.e., they should replicate the bone tissue architecture in order to favor implant integration as much as possible [22], [23]. Natural bone has complex and irregular pores with irregular surface morphology and a spread pore size distribution [36]. To mimic these features, the state-of-the-art scaffolds are designed and manufactured relying on mesh-fiber geometries, squared cells, or, with enhanced biomimetic features, using implicit surface, such as Triply Periodic Minimal Surfaces (TPMS) [36]. Indeed, the use of implicit surfaces bone scaffolds has the advantages of providing large and complex topological structures [36]. Furthermore, TPMS-based scaffolds demonstrated increase permeability to body fluids and nutrients (10^{-8} m^2vs. an average of about $10^{-9}m^2$) [37]. The mechanical properties of TPMS architecture resulted in an effective elastic

TABLE 1. Summary of triply periodic minimal surfaces (TPMS) and associated function used in scaffold design.

Surface	Function (F)
P	$\cos(X)+\cos(Y)+\cos(Z)=k$
D	$\cos(X)\cos(Y)\cos(Z)-\sin(X)\sin(Y)\sin(Z)=k$
G	$\sin(X)\cos(Y)+\sin(Z)\cos(X)+\sin(Y)\cos(Z)=k$
I-WP	$2[\cos(X)\cos(Y)+\cos(Y)\cos(Z)+\cos(Z)\cos(X)]-[\cos(2X)+\cos(2Y)+\cos(2Z)]=k$
L	$0.5[\sin(2X)\cos(Y)\sin(Z)+\sin(2Y)\cos(Z)\sin(X)+\sin(2Z)\cos(X)\sin(Y)]$ $-0.5[\cos(2X)\cos(2Y)+\cos(2Y)\cos(2Z)+\cos(2Z)\cos(2X)]+0.15=k$

modulus higher than their standard counterparts (e.g., fiber meshes) [38], for lower porosity values, while ensuring a better stress distribution [39], [40]. All these features made the TPMS architecture very appealing for developing bone scaffolds [37], [41]–[44]. In this framework, given the foreseen application of using TPMS MagS as devices for performing HT of bone tumors, it is mandatory to assess the influence of the geometry on the local heating administration.

This work aims to investigate how and if the scaffold architecture can affect the hyperthermic potential of magnetic scaffolds. We propose a simple but effective methodology for designing TPMS scaffolds. Then we 3D printed three types of implants with a commercial poly-lactic acid (PLA) filled with magnetite microparticles. The samples were characterized in terms of physical properties and of heating potential, under different experimental conditions. The experimental setup was supported by extensive numerical multiphysics simulations.

The work is organized as follows. In Sect. II we describe the methodology for obtaining a solid scaffold starting from the mathematical representation of triply periodic minimal surfaces. In Sect. III we report the methods used for characterizing the TPMS MagS. In Sect. IV results are presented and they are discussed in Sect. V.

II. SCAFFOLD DESIGN

A. TRIPLY PERIODIC MINIMAL SURFACES

TPMS is a surface embedded on R^3 which is minimal (i.e., with a mean curvature equal to zero) and it is periodic on the three directions x, y, z. TMPS can be modelled by using the Enneper-Weierstrass parametric representation [36], [44]–[46]. Among the different approaches for generating the TPMS coordinates, the parameterization of this kind of surfaces in the complex domain is not a straightforward and suitable approach for the computational representation [36]. Indeed, in the Euclidean space, the TMPS can be approximated by an implicit function, i.e., as a level surface (isosurface) of a function F: $R^3 \rightarrow R$ which is a combination of sinus and cosine. The most famous and useful functions for generating TMPS for biomedical applications are reported in Tab. 1 [36], [42], where $X = w_x x$, $Y = w_y y$ and $Z = w_z z$, being w_x, w_y and w_z the spatial periods and k is a constant.

TPMS possess two important mathematical properties: minimality and periodicity. For a computationally efficient Computer Aided Design (CAD) it is of relevance to discuss them. A pivotal aspect is the minimality of TPMS. In order to verify this feature, the mean curvature for surfaces in implicit form can be used [47]:

$$K_M = \frac{\nabla(F)\, H(F)\, \nabla(F)^T\, |\nabla(F)\,\mathrm{Trace}(H)|}{|\nabla(F)|^3} \tag{1}$$

where $\nabla(F)$ is the gradient, $H(F)$ is the Hessian matrix and $\mathrm{Trace}(H)$ is the trace of $H(F)$ of the arbitrary function from Tab. 1. Minimality ensures very good mechanical properties and a stiffness suitable for orthopedic applications, while minimizing the amount of material used for scaffold manufacturing (e.g., in 3D printing or sintering) [36], [48]–[50]. The other relevant mathematical property is periodicity. Indeed, since TMPS are level surfaces of harmonic functions, they inherit their periodicity in a given domain. The periodicity simplifies noticeably the computation and the repetition of a unit cell to develop a solid from TPMS, allowing to extend it indefinitely in space [36].

However, for clinical purposes and for the goal of this work, the representation should be biomimetic and suitable for manufacturing the proposed new type of multifunctional therapeutic orthopaedic devices.

B. SCAFFOLD STRUCTURING: DEFORMATION

Since the surgical resection of bone tumors leave a gap, which must be filled with the scaffold, as shown in Fig. 1, it is necessary to provide the implant in a suitable shape, in order to simplify and adapt the scaffold to the surgically treated bone boundaries [20], [36]. In previous studies it was shown that it is possible to design a solid from TPMS within a shape of arbitrary boundaries starting from the deformation of a parallelepiped [36], [42]. From a mathematical point of view, this implies that a continuous function f_t from the defected bone boundaries to the parallelepiped exists. Supposing that the defect shape can be approximated to a cylinder, which is fit to long bones, the transformation law is $f_t : \boldsymbol{R}^3 \rightarrow \boldsymbol{R}^3$ and can be expressed as:

$$\begin{cases} (0,0,z) & x^2+y^2=0 \\ \left(\dfrac{x\cdot\max\{|x|,|y|\}}{\sqrt{x^2+y^2}}, \dfrac{y\cdot\max\{|x|,|y|\}}{\sqrt{x^2+y^2}}, z\right) & x^2+y^2\neq 0 \end{cases} \tag{2}$$

An example of the transformation using Eq. (2) is show in Fig. 2.a. The transformation is necessary since usually the computational domain is $[x_0, x_1] \times [y_0, y_1] \times [z_0, z_1]$. Eq. (2) can be applied directly to a TPMS, as shown in Fig. 2.b. The

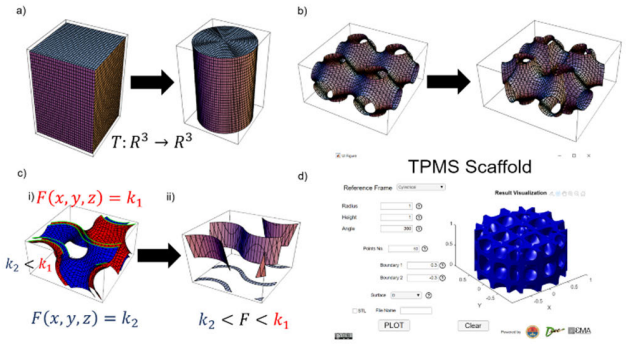

FIGURE 2. Description of the steps for deriving scaffolds based on solid triply periodic minimal surfaces (TPMS) architecture: a) Transformation of the parallelepiped frame into cylinder: the two objects have the same height while the parallelepiped base, a square with side l, is transformed into a circle with $l/2$ radius. b) Transformation applied to a P-surface in $[-1, 1]^2 \times [0, 1]$. c) i. The inner and the external G-Surface plotted in $[0, 1]^2 \times [0, 1/2]$. ii. Closure surfaces and borders of the sections (green curves). d) Example of the developed GUI: final solid scaffold based on a D-surfaces.

output is a surface, not a solid. Therefore, it is necessary to create a volume. In other words, an unclosed implicit surface can be closed only if one or more intersecting surfaces can be found, which is the utmost issue for the structuring of a curved surface in three-dimensional space [36].

C. SOLID FORMATION

By using the software Matlab 2019b (The MathWorks Inc., Boston USA) [51], the ''TPMS Scaffold'' application was developed for deriving TPMS scaffolds. Given a TPMS surface with law F from Tab. 1, it is possible to generate a solid volume by creating two offset surfaces, an inner and an outer one, which must be linked and closed to form the final solid, porous biomimetic architecture for bone tumor treatment. The proposed graphic user interface (GUI) allows to choose among the TPMS from Tab. 1, compute the two offset surfaces by using the ''isosurface'' function and derive the final solid in ''.stl'' format [52]. To respect the minimality and speed up the computation, instead of working on each mesh polygons [36], we select two constants $k_1 > k_2$ and a height $0 < h < 1$. The inner surface is $F(x, y, z) = k_2$, whilst $F(x, y, z) = k_1$ is the external one, as shown in Fig. 2(c). In order to derive the solid, the surface junction between them at the height h is the set of points which satisfies the inequality $k_2 < F(x, y, z) < k_1$. The set of surface boundary points is triangulated [36] and the convex hull is found for the inner and outer surface, then, the redundant, intersecting and non-manifolds triangles are removed, and the closing surfaces are found, as shown in Fig. 2(c). Thus, the solid TPMS-based scaffold with a cylindrical bone-fit shape is obtained, as shown in Fig. 2(d).

D. 3D PRINTING

The commercial magnetic-polymer composite filament Magnetic Iron PLA purchased from Proto-Pasta [53] was used to print the magnetic thermo-seeds samples. The filament consists of 40 wt.% of iron microparticles (40 μm in size) loaded in a polylactic acid (PLA) polymer matrix (NatureWork's 4043D Ingeo Biopolymer) [54], [55].

TABLE 2. Summary of magnetic scaffold geometries.

Sample	Geom.	Avg. pore size (mm)	Ferromagnetic (Y/N)	Weight (g)
S1	90°-SF	0.35	N	2.00
S1F	90°-SF	0.35	Y	3.70
S2, S3	G surf.	0.3	N	0.85
S2F, S3F	G surf.	0.3	Y	1.42
S4, S5	L surf.	0.32	N	2.18
S4F, S5F	L surf.	0.32	Y	3.20

90°SF = 90°-Shifted fiber scaffold, G surf. = Gyroid TPMS surface, L surf. = Lidinoid Surface TPMS = Triply Periodic Minimal Surface

The sample geometry was checked using Rhinoceros v7 (McNeel, Canada) modeling software, then the IdeaMaker software was used to derive the stereolithography (STL) files and the g-code for printing them with the Raise3D Pro2 Plus 3-D printer. The extrusion temperature was set to 210°C for the 0.45 mm nozzle, with a 100% infill density and a 50 mm·s^1 printing speed. The bed temperature was set to 45°C. As a reference geometry, we printed a standard 90°-shifted mesh scaffold (S1, S1F). We printed two G-surface (S2, S3, S2F, S3F) and two L-surface (S4, S5, S4F, S5F) scaffolds, having size 1.8 cm × 1.8 cm × 2.5 cm, using non-magnetic and iron-filed PLA. A summary of their geometrical features is provided in Tab. 2. The samples are shown in Fig. 3.a.i top row shows SiF (with $i = 1, 2, \ldots, 5$) scaffolds printed with the Fe-PLA Proto-Pasta filament and bottom row Si reference scaffolds printed with a typical PLA non-magnetic filament.

III. CHARACTERIZATION

A. STATIC MAGNETIC MEASUREMENTS

Magnetic hysteresis loops of the magnetic filament were recorded at 300 K using an Oxford Instruments 1.2H/CF/HT Vibrating Sample Magnetometer (VSM), for magnetic field strengths ranging from -1 to 1 T.

B. THERMOGRAVIMETRIC ANALYSIS AND SPECIFIC HEAT MEASUREMENTS

The simultaneous Differential Scanning Calorimeter (DSC)-Thermogravimetric (TGA) analyzer Q600M (TA, New Castle, DE) was used to quantify the thermal stability and the content of magnetic phase in the filament after thermal degradation [55]–[59]. A 40μl alumina pan was used as a sample holder. The same type of alumina pan is employed as reference material during the differential measurement. The initial temperature was 20°C. The protocol consists of a heating ramp with a slope of 20°C·min^{-1} up to the final temperature of 1000°C. The temperature values at different

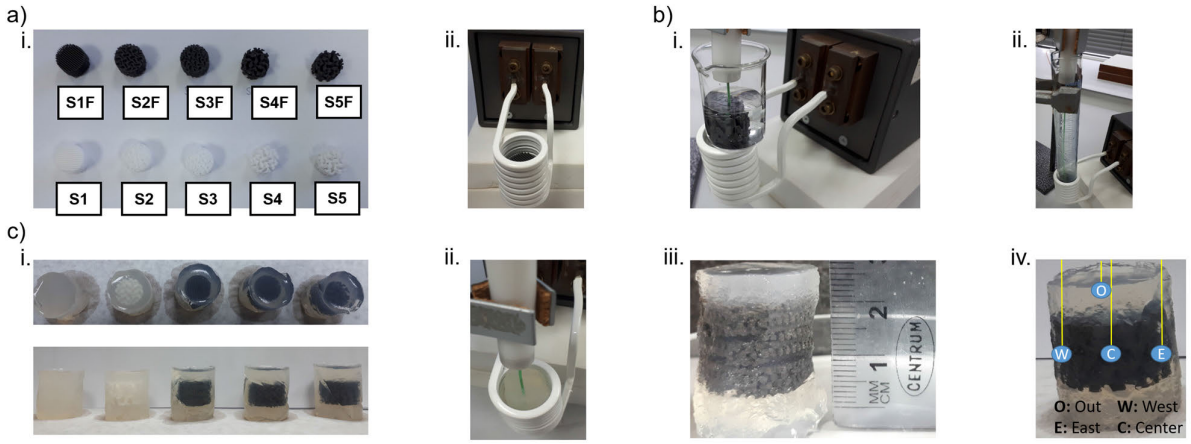

FIGURE 3. a) i. Optical images of the Fe-PLA Proto-Pasta magnetic scaffolds with TPMS architecture, top line and identical PLA scaffolds. ii. In-air or free space setup: experimental induction heating apparatus and sample placement. b) i. Sample placed in a beaker filled with distilled water, outside the induction heating coil. ii. Sample placed in distilled water inside the induction heating coil. c) Top-view of the agar phantom-scaffold systems. ii. Side view of the agar phantom-scaffold systems. iii. Dimensions of the agar phantom. iv. Details of the measurements site inside the sample and in the agar phantom.

mass percentage (T20%, T50%, T90%) are considered. The first derivative of the weight vs. temperature was investigated for the thermal degradation analysis. From the DSC-TGA analysis, the content of the magnetic phase dispersed in the polymeric matrix is analyzed and used as information to complement the estimation of dissipated power during the hyperthermia treatment.

In order to simulate and gain insights into the heat transfer phenomena occurring during the HT of bone tumors, performed using the commercial magnetic filament under analysis, we characterized the filament in terms of its specific heat (C_p). Indeed, the thermal conductivity of the Proto-Pasta filament was measured in [55] and a value of $\sim$0.47 $W{\cdot}m^{-1}K^{-1}$ was reported. In this framework, we adopted the measurement methods from the ASTME1269-11 standard [60]. In detail, we performed a blank run, then a reference run with alumina standard was performed for the baseline removal and, finally, a run with the magnetic sample, placed in good contact with the 40 μl pan, was carried out by heating the sample from 15°C to 70°C, using a heating rate of 10°C/min.

C. EXPERIMENTAL EVALUATION OF SPECIFIC ABSORPTION RATE

As discussed in the introduction, several works dealt with the experimental characterization of the hyperthermic potential of magnetic scaffolds for bone tissue engineering [1], [3], [11], [24], [25], [35]. However, taking a look into the methodologies, conditions and setup used for the calorimetric measurements of this kind of solid samples embedding magnetic particles, it is possible to underline that the good practices, recommendations and standardization developed for MNPs characterization were neglected or scarcely adopted [61]–[63]. However, MagS, being implantable medical devices to be used as heat source in the interstitial hyperthermia treatment of bone tumors, must follow the recently released requirements for [64]. Therefore, more robust, accurate and in-depth characterization is required.

All samples from Fig. 3.a.i were placed in the middle of an 8-turn coil, having a 2.53 cm diameter and 4.3 cm height. The induction heating system is the EASYHEAT 1.2 kW from Ambrell. The derivation of the specific absorption rate (SAR) is performed followed the strategy from [61], [65], based on the modified law of cooling in order to reduce the uncertainties due to measuring conditions and experimental setup. Typically, the envelope of the external magnetic field is turned-off at a given time in order to allow the thermal recovery of the system. Coil cooling water temperature was kept stable at 18.9°C during whole experimental procedure.

Three different experimental setups were considered. First, the 3D printed TPMS scaffold was exposed to the induction heating system in air. An infrared (IR) camera (FLIR i3, FLIR Systems, USA) was used to acquire images, from which the average scaffold temperature is derived. Then, the magnetic scaffold was placed in distilled water, as shown in Fig. 3.b. Approximately 5 mL of distilled water was used as the solution medium. The field amplitude was increased to 30 mT and the working frequency was 400 kHz ($|\boldsymbol{H}| \times f = 9.5{\cdot}10^9$ $Am^{-1}s^{-1}$). Five symmetrical holes were opened to place the optical fiber for temperature recording (Fig. 3.b). Finally, the printed magnetic scaffolds were incorporated in an agarose (10 $mg{\cdot}ml^{-1}$) phantom system, as shown in Fig. 3.c.i The phantom agar is supposed to better mimic the biological environment [61]. Pure agarose phantom and sample S4 were used as reference samples.

IV. NUMERICAL ANALYSIS

Given the extensive characterization of TPMS magnetic scaffolds, we developed a numerical framework for simulating the multiphysics phenomena related to the calorimetric measurements. In this framework, we aim to corroborate the experimental findings and refine the problem of modeling these functional biomaterials, thus paving the way for coping with the issue of planning the treatment with these innovative

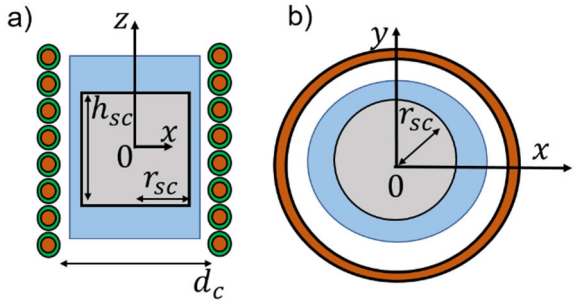

FIGURE 4. Sketch of the geometry used for simulating the experimental setup of the calorimetric measurements of the magnetic scaffolds: a) *zx*-view and b) *xy* -view. The cylinder in light blue can be either air, water or agar.

TABLE 3. Materials EM and thermal properties for the simulations.

Mat.	ε_r	μ_r	σ (Sm^{-1})	k ($Wm^{-2}K^{-1}$)	C_p ($Jg^{-1}C^{-1}$)	ρ ($kg{\cdot}m^{-3}$)
Air	1	1	0	-	-	-
Agar	70	1	0.2[67]	0.48	4.000 [67], [68]	1000[67]
Copper	-	1	$5{\cdot}10^7$	-	-	-
PLA	2.5	1	10^{-6}	0.29 [54]	1.800 [69]	900[55]
Fe-PLA	3	8	10^{-5}	0.47 [54]	~1.240	2745[54]
Distilled Water	76	1	$5{\cdot}10^{-6}$	0.57 [67]	4.200 [67]	1050[67]

devices [66], [67]. To this aim, a simplified geometry was assumed.

The finite element method (FEM) commercial software Comsol Multiphysics v5.5 (Comsol Inc., Burlinghton, MA USA) was used to simulate the experimental setup for the specific absorption rate measurements, in the case of a homogeneous cylindrical scaffold made with the Proto-Pasta magnetic PLA. In detail, for the system geometry shown in Fig. 4, we solved the electromagnetic problem making use of the *AC/DC* module in the frequency domain, under the assumption of a quasi-static process. The solution of the Maxwells' equation through the vector potential formulation allows to compute the magnetic field produced by the 8-turn copper coil (coil diameter $d_c = 2.54$ cm, height $h_c = 4.3$ cm, coil wire diameter $d_{sc} = 0.53$ cm) inside the sample and the background media, which can be air, or water or agar (see Fig. 3). The power dissipated by the magnetic scaffolds (P_m) is evaluated as:

$$P_m = fA_{hyst} \tag{3}$$

where f is the working frequency (in Hz) and A_{hyst} is the area of the hysteresis loop derived from the static magnetic measurements (in J), scaled by the specific density of the scaffold sample. The local and time-varying magnetic field is considered for computing Eq. (3).

The total electromagnetic power (P_{EM}) dissipated by the ferromagnetic scaffold is used as source term for the unsteady Fourier's equation [61], [65]–[67] from which the spatial and temporal dynamics of the temperature field inside the sample are computed. In mathematical terms

$$\rho C_p \frac{\partial T}{\partial t} = \nabla \cdot (k \nabla T) - \boldsymbol{u} \cdot \nabla T + P_{EM} \tag{4}$$

where ρ is the material density ($kg{\cdot}m^{-3}$), C_p is the specific heat capacity ($J{\cdot}kg^{-1}K^{-1}$), whilst k is the thermal conductivity ($W{\cdot}m^{-1}K^{-1}$). The physical properties of the samples are reported in Tab. 3 [68]–[70]. The *Heat Transfer in Solid* module was used.

In the general heat transfer balance (4), $\boldsymbol{u}$ is the convective velocity field vector ($m{\cdot}s^{-1}$). The form and nature of this term depends upon the experimental conditions. Therefore, a clarification is needed. For the thermographic measurements performed in air (Fig. 3.a), and in the case of the in-agar setup (Fig. 3.c), the external boundaries of the sample or agar exchange heat by convection with the surrounding air ($T_{air} = 20°C$), i.e.

$$-\boldsymbol{n} \cdot \nabla T = h_{air} (T - T_{air}) \tag{5}$$

Being $\boldsymbol{n}$ the normal vector. The heat transfer coefficient (h_{air}) is derived from the cooling phase of the experimental heating curves. As a result, the heat transfer problem for the free space and in-agar experimental setups (Fig. 3.a and 3.c) was modeled as an unsteady heat conduction problem (i.e., $\boldsymbol{u} = \boldsymbol{0}, \forall x, y, z$).

Instead, for MagS placed in distilled water, as shown in Fig. 3.b, the heat transfer problem was assumed to be non-linear by taking into account the convective motion due to the temperature gradients in the system ($\boldsymbol{u} \neq \boldsymbol{0}$). Therefore, the Navier-Stokes equation was solved coupled to the Fourier's partial differential equation [71], [72]

$$\begin{aligned} \rho \frac{\partial \boldsymbol{u}}{\partial t} + \rho (\boldsymbol{u} \cdot \nabla) \boldsymbol{u} &= \nabla \cdot \left[-P\boldsymbol{I} + \eta \left(\nabla \boldsymbol{u} + (\nabla \boldsymbol{u})^T \right) \right. \\ &\quad \left. - \frac{2}{3} \eta (\nabla \cdot \boldsymbol{u}) \boldsymbol{I} \right] = 0 \\ \rho \frac{\partial \boldsymbol{u}}{\partial t} + \nabla \cdot (\rho \boldsymbol{u}) &= 0 \end{aligned} \tag{6}$$

where η is the dynamic viscosity (equal to 1 cP for water) and $\boldsymbol{I}$ is the identity matrix. Eq. (4) is subject to an open boundary condition at the water-air interface ($-\boldsymbol{n} \cdot \boldsymbol{u} = 0$) and no-slip condition at the inner surfaces of the vial surfaces ($\boldsymbol{u} = 0$). The *Laminar Flow* interface was used.

With the temperature field computed from the solution of Eq. (4), the SAR is evaluated as [61], [65]:

$$SAR = \frac{w_a}{w_{sc}} C_{p,agar} \frac{\Delta T}{\Delta t} \tag{7}$$

where w_a and w_{sc} are the agar and scaffold mass (in g), respectively, whilst $\frac{\Delta T}{\Delta t}$ is the initial slope of the heating curve. The interval Δt is on the order of tens of seconds [61].

V. RESULTS

From the curve of magnetization versus magnetic flux density shown in Fig. 5.a, it is possible to notice that the magnetic filament presents a relatively small coercive force of

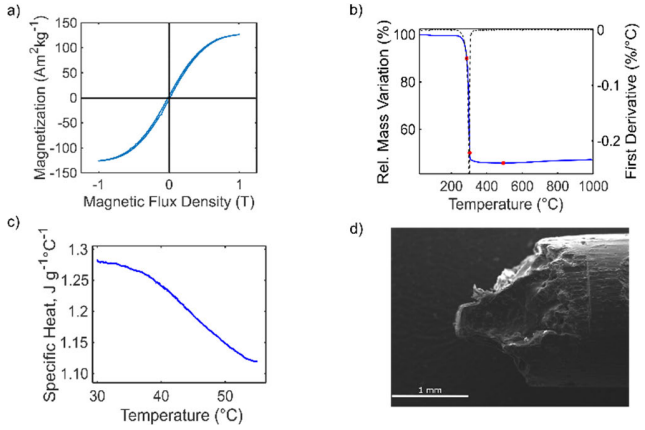

FIGURE 5. a) Magnetization (Am^2kg^{-1}) of the Iron-PLA Proto-Pasta filament, before printing, as a function of the external applied magnetic flux density field (T). The residual magnetic flux density is about 12.5 mT and the saturation magnetization is ∼126 Am^2kg^{-1}. b) Thermogravimetric analysis (TGA) of the Fe-PLA Proto-Pasta filament, in the range 20°C-1000°C. The normalized weight (%) and the first derivative over temperature are presented. c) Specific heat ($Jg^{-1}C^{-1}$) of Fe-PLA Proto-Pasta filament in the temperature range 30-60°C. d) Scanning Electron Microscope (SEM) images of the Iron-PLA Proto-Pasta fibers at different magnifications.

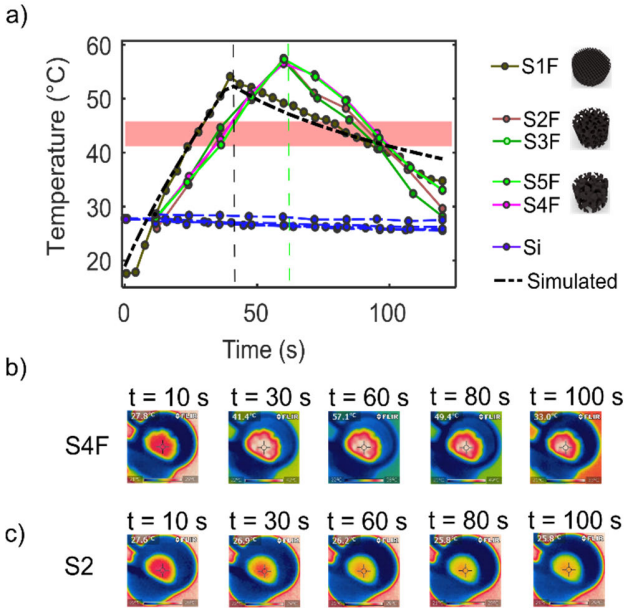

FIGURE 6. a) Temperature profiles for PLA and Fe-PLA TPMS scaffolds placed in the coil in air, and compared to the simulation results (dash-dot line). The vertical dashed lines highlight the time point at which the external magnetic field is turned off. The average temperature is derived from the thermographic images. Examples of the b) S4F and c) S2 samples are shown.

12.5 mT, with a small loop, similar to soft ferromagnets, and a saturation magnetization (M_s) of about 126 $A{\cdot}m^2{\cdot}kg^{-1}$. M_s indicates the ratio of iron to PLA in filament, considering that bulk iron's M_s is 220 $A{\cdot}m^2{\cdot}kg^{-1}$. This finding is also in perfect agreement with the magnetic response data of the filament and of 3D printed items with 1-2 layers, a 100% infill density reported by [54]. The amount of magnetic phase and the distribution along the fiber were assessed by DSC-TGA and microscopy. Indeed, from Fig. 5.b, it is possible to notice a 50% primary loss at a temperature of about 303°C which corresponds to the thermal degradation of the PLA matrix [58]–[60], as confirmed by the analysis of the first derivative of the sample weight with respect to the temperature. The residual mass at 600°C is about 45.67% of the initial weight, which correspond to the amount of non-organic crystalline phase of the iron in the filament, observed also in SEM images (Fig. 5.d).

In Fig. 5.c the specific heat of the magnetic polymer is shown. In the temperature range typical of the HT of bone tumors with magnetic scaffolds [67], the composite material can store an energy per amount of mass and temperature of about 1.24 $J{\cdot}g^{-1}{\cdot}C^{-1}$, on average, which is approximately the value estimable assuming a linear, volumetric mixing between magnetite and PLA (∼4.8% difference) [71]. In this work the quadratic temperature dependence of the physical properties, given a variation of ∼0.6%·°C^{-1}, is neglected in the simulations to solve a linear problem and hence lower the computational burden.

The curves of temperature versus time acquired by IR thermography for the five magnetic scaffolds (and their nonmagnetic counterparts), in air, exposed to a 15 mT magnetic field, working at 400 kHz, are reported in Fig. 6. The bare PLA samples do not heat up, given the low electrical conductivity (see Tab. 3), but tend to equilibrate their temperature with air. Furthermore, it is possible to notice that the maximum temperature is about 56.5 ± 1.5 °C and it is reached in about 55 ± 5 s, for S3F, S4F and S5F samples. Between the standard 90°-shifted mesh magnetic scaffold (S1F) and the TPMS architectures differences in the peak temperatures and in the cooling rate with the surrounding medium can be observed in Fig. 6. Furthermore, the simulated time evolution of the average temperatures for a homogeneous cylindrical magnetic scaffold is very similar to that of scaffolds S1F, as shown in Fig. 6. The discrepancy between the numerical simulations and the temperature profiles of TPMS MagS is probably due to the geometric features and the sample porosity. From the findings of Fig. 6, the Proto-Pasta ferromagnetic scaffolds look very promising for magnetic hyperthermia application. However, this experimental configuration is not very representative of the in vitro or in vivo-like thermal and electromagnetic environment experienced during the interstitial hyperthermia treatment (Fig. 1).

To better mimic the hyperthermia treatment typical of hyperthermia, we placed the magnetic scaffolds samples inside 5 mL of distilled water, (Fig. 3.b) in a glass container, and recorded the temperature by placing an optical fiber at the top surface of the material opening the five holes shown in Fig. 3.b. With respect to the in-air setup, the field amplitude was increased to 30 mT in order to reach the same temperatures. The measured temperature profiles are reported in Fig. 7. The reference architecture S1F can heat up the water to 56 ± 2°C. The simulated temperature profile for the non-linear heat transfer of the homogenous ferromagnetic cylinder exposed to the RF magnetic field are very similar to that of S1F sample, as shown Fig. 7. From the modified law

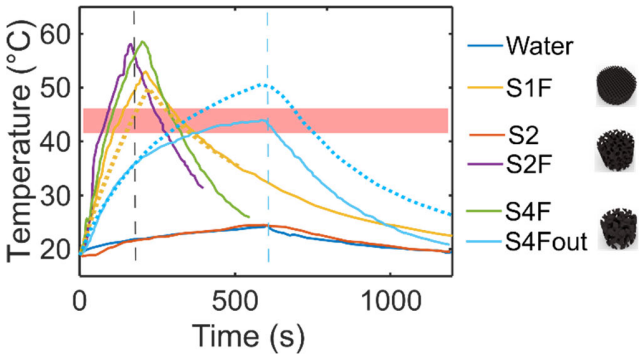

FIGURE 7. Temperature profiles of S1F, S2F and S4F scaffolds in distilled water, exposed to a 30 mT magnetic field, working at 400 kHz. The thermal response of the water environment is also reported. The non-magnetic polymeric equivalent is always tested for comparison. The solid lines are the measurements, and the dashed lines are the simulated cases. The vertical dashed lines highlight the time point at which the external magnetic field is turned off.

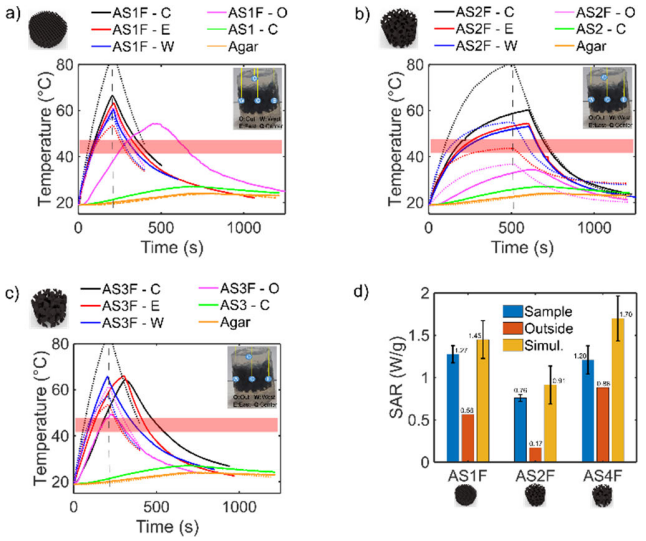

FIGURE 8. Temperature profiles in agar for a) S1F scaffold (90°-mesh), b) S2F scaffold (Gyroid) and c) S4F scaffold (L-surface), and comparison with the multiphysics simulations (dashed lines), for an external field of $B_0 = 30$ mT and $f = 400$ kHz. The vertical lines highlight the time point at which the external magnetic field is turned off. d) Estimated specific absorption rate (SAR) values in the sample and in the phantom (Outside).

of cooling, and taking into account the response of the environment, we can notice that the L-surface scaffold (S4F) can reach the maximum temperature of 59°C in ∼200 s, whilst the gyroid architecture (S2F) could raise the temperature to 45°C. The heating and cooling rate are faster for S2F and S1F, if compared to S1F and the simulated homogeneous case. The fact that the TPMS architecture experience a different heat transfer regime is also epitomized by the comparison of the temperature pattern of SF4 sample placed just outside the coil (see Fig. 7). Even though the convective motion of water is considered, the numerical simulations fail in reproducing the experimental results.

From Fig. 7, all ferromagnetic scaffold samples succeeded to surpass the hyperthermia temperature limit within 10 min or earlier. However, from these calorimetric measurements, we can infer that the heating efficiency varies due to material quantity. Indeed, by weighting the samples we could better explain the heating behavior, since S1F, S2F and S4F weight 3.7 g, 1.4 g and 3.2 g, respectively (Tab. 2). Furthermore, additional uncertainty about the temperature values may arise from the temperature probe placement. Therefore, it is worth noting that the SAR values can be estimated after standardizing the experiment. Hence, given these findings in this setup, we must underline that the selection of the most promising architecture requires additional considerations.

To the aim of refining the experimental condition for assessing the hyperthermic potential of ferromagnetic TPMS scaffolds, we used agarose gel as a medium to mimic the electromagnetic and heat transfer environment of biological tissues [33]. As shown in Fig. 3, for lowering the influence of the probe placement on the measured temperature, five different optical fibers positions were selected in order to provide more reliable temperature and SAR results. The measured temperatures in the five locations inside the sample and the agar phantoms, for each ferromagnetic scaffold, are reported in Fig. 8. A large variability of the peak temperature in the sample is noticed: for the S1F, an average temperature of 61.5 ± 3°C, for S2F 55 ± 4°C and for S4F 64.6 ± 7°C. The highest temperatures were recorded in the center of the samples for S1F and S2F, but not for S4F, which presented a relevant homogeneity in terms of heating. The numerical simulations, on the other hand, overestimate the temperature in the sample center, while the simulated profiles for all the samples are fit with the measurements in W and E location points (Fig. 8). By carefully analyzing Fig. 8.a-.c, it can be noticed that at about 5 mm away from the MagS surface, the temperature decay, and the thermal gradient, can be relevant. Indeed, S1F showed a 5.5°C decrease, whilst S2F a ∼24°C reduction and S4F a ∼14.6°C lowering. In this framework, given the different temperature rises, during the evaluation of the hyperthermic potential of these ferromagnetic TPMS scaffolds, an averaging procedure must be taken into account in future studies.

With the recorded temperature profiles, according to Eq. (7), we evaluated the specific absorption rate per mass unit of agar. The results are reported in Fig. 8.d. It is possible to notice that the scaffold SAR estimated by averaging the five measurements inside the sample ranges from 0.8 $W \cdot g^{-1}$ to 1.3 $W \cdot g^{-1}$ (Fig. 8.d). On the other hand, when measuring outside the scaffold volume (point O in Fig. 3.c), the SAR levels ranges from 0.17 $W \cdot g^{-1}$ to 0.88 $W \cdot g^{-1}$ (Fig. 8.d). The SAR estimated from the numerical simulation tends to overestimate the measured value, but, considering the large temperature variation in the sample volume, the in silico findings overlap with the measured values, resulting in a maximum difference of ∼0.5 $W \cdot g^{-1}$ from the experimental levels. The SAR findings given in Fig. 8.d indicates that the different scaffold architecture can slightly affect the average hyperthermic potential. Indeed, the estimated SAR values are enough for ensuring an effective interstitial hyperthermia treatment, according to [63], since at least 0.5 $W \cdot g^{-1}$ must be

deposited in the target tumor volume. Even though the SAR level of MagS are about one order of magnitude lower than those reported for ferrofluids [61]–[65], they are comparable to the other literature measurements. A tee glass ceramic scaffold embedding $ZnFe_2O_4$ particles, tested in deionized water, under the action of a 100 kHz and 50 mT, resulted in 5 W per gram of sample [74]. For a 3D-printed poly-caprolactone and mesoporous bioactive glass scaffold containing magnetite nanoparticles, exposed to a 409 kHz and 18 mT magnetic field, the SAR fells within 1.4-4.7 $W{\cdot}g^{-1}$ [75]. However, the experimental setups, the exposure conditions, the thermometry and the methodology for estimating the SAR from [74] and [75] differs from that investigated and proposed in this work. These results, and the comparison with the literature, also demonstrate that the estimation of the SAR of MagS requires further numerical and more accurate experimental analysis.

VI. CONCLUSION

Bone cancers are aggressive and incapacitating pathologies which requires innovative therapeutic modalities to: i) avoid limb sparing surgery or facilitate the post-operative bone healing, ii) to increase the effectiveness of chemo- and radiotherapy in order to enhance the survival rate, and iii) to control the local recurrence rate. A promising solution is the use of properly designed multifunctional magnetic biomaterials as prosthetic implant to be used after tumor resection for i) favoring the bone repair and healing and ii) performing, on demand, by the remote application of an external radiofrequency magnetic field, the hyperthermia treatment for eliminating the potential residual cancer cells, favoring other therapeutic modalities.

In this work, we designed and characterized biomimetic, magnetic scaffolds based on triply periodic minimal surfaces to be used for the hyperthermia treatment of bone tumors. A GUI was developed for deriving printable models for TPMS scaffolds. The proposed computational geometry approach can be extended to derive prosthetic implants of realistic shape, with controlled porosity and osteogenic potential [36]. Then, a set of potential MagS was 3D printed by FDM using a commercial PLA filled with iron particles. This work investigated for the first time the possibility of using this commercial product as a tool for manufacturing biomedical magneto-responsive devices. The static magnetic properties of the magnetic polymer were investigated by their hysteresis loop, which exhibit soft magnetic features typical of ferromagnet. The thermal stability and the specific heat of the material were analyzed through DSC-TGA. The heating evaluation of 3D-printed ferromagnetic samples were examined in magnetic hyperthermia application. To the best of the authors' knowledge, for the first time we analyzed if the TPMS scaffold architecture could be used as local heater for performing the interstitial HT of bone tumors and investigated if the geometric features could have an influence to the treatment outcome. In this framework, several different experimental setups were considered: different media and thermometric methods were evaluated (i.e., IR camera (no medium) and optical fiber (distilled water or agarose gel) were chosen as case studies). The temperature values were recorded at different samples positions to have reliable SAR results. All MagS samples succeeded to surpass the hyperthermia temperature limit within 10 min or earlier. Using agarose gel as a medium is the most accurate way to estimate the scaffolds heating efficiency. The simulations and measurements highlight that the temperature curves and the specific absorption rates are dependent upon the placement of the optic fiber in the sample, resulting in an average difference of 5°C in 1 cm.

These findings highlight the need of further works devoted to the assessment of MagS biocompatibility and iron particle release [8], [12], and devoted to development of standardized protocols for calorimetric measurements of solid nanocomposites magnetic implant for interstitial hyperthermia [76], [77]. In particular, in spite of the recent advancements and discussion about the characterization of magnetic ferrofluids [61]–[63], future works must deal with the development of a standardized protocol or a set of guidelines for performing reliable, reproducible and accurate measurements of the hyperthermia potential of magnetic scaffolds for tumor treatment.

ACKNOWLEDGMENT

(Matteo Bruno Lodi and Antonis Makridis contributed equally to this work.)

REFERENCES

[1] A. Farzin, M. Fathi, and R. Emadi, "Multifunctional magnetic nanostructured hardystonite scaffold for hyperthermia, drug delivery and tissue engineering applications," *Mater. Sci. Eng., C*, vol. 70, pp. 21–31, Jan. 2017.

[2] A. Russo, M. Bianchi, M. Sartori, M. Boi, G. Giavaresi, D. M. Salter, M. Jelic, M. C. Maltarello, A. Ortolani, S. Sprio, M. Fini, A. Tampieri, and M. Marcacci, "Bone regeneration in a rabbit critical femoral defect by means of magnetic hydroxyapatite macroporous scaffolds," *J. Biomed. Mater. Res. B, Appl. Biomater.*, vol. 106, no. 2, pp. 546–554, Feb. 2018.

[3] S. Dong, Y. Chen, L. Yu, K. Lin, and X. Wang, "Magnetic hyperthermia–synergistic H_2O_2 self-sufficient catalytic suppression of osteosarcoma with enhanced bone-regeneration bioactivity by 3D-printing composite scaffolds," *Adv. Funct. Mater.*, vol. 30, no. 4, Jan. 2020, Art. no. 1907071.

[4] R. De Santis, A. Russo, A. Gloria, U. D'Amora, T. Russo, S. Panseri, M. Sandri, A. Tampieri, M. Marcacci, V. A. Dediu, C. J. Wilde, and L. Ambrosio, "Towards the design of 3D fiber-deposited poly(-caprolactone)/iron-doped hydroxyapatite nanocomposite magnetic scaffolds for bone regeneration," *J. Biomed. Nanotechnol.*, vol. 11, no. 7, pp. 1236–1246, Jul. 2015.

[5] E. Díaz, M. B. Valle, S. Ribeiro, S. Lanceros-Mendez, and J. M. Barandiarán, "A new approach for the fabrication of cytocompatible PLLA-magnetite nanoparticle composite scaffolds," *Int. J. Mol. Sci.*, vol. 20, no. 19, p. 4664, Sep. 2019.

[6] D. Mertz, S. Harlepp, J. Goetz, D. Bégin, G. Schlatter, S. Bégin-Colin, and A. Hébraud, "Nanocomposite polymer scaffolds responding under external stimuli for drug delivery and tissue engineering applications," *Adv. Therapeutics*, vol. 3, no. 2, Feb. 2020, Art. no. 1900143.

[7] Y. Li, G. Huang, X. Zhang, B. Li, Y. Chen, T. Lu, T. J. Lu, and F. Xu, "Magnetic hydrogels and their potential biomedical applications," *Adv. Funct. Mater.*, vol. 23, no. 6, pp. 660–672, Feb. 2013.

[8] H.-Y. Xu and N. Gu, "Magnetic responsive scaffolds and magnetic fields in bone repair and regeneration," *Frontiers Mater. Sci.*, vol. 8, no. 1, pp. 20–31, Mar. 2014.

[9] A. A. Adedoyin and A. K. Ekenseair, "Biomedical applications of magneto-responsive scaffolds," *Nano Res.*, vol. 11, no. 10, pp. 5049–5064, Oct. 2018.

[10] B. Smolková, M. Uzhytchak, A. Lynnyk, Š. Kubinová, A. Dejneka, and O. Lunov, "A critical review on selected external physical cues and modulation of cell behavior: Magnetic nanoparticles, non-thermal plasma and lasers," *J. Funct. Biomater.*, vol. 10, no. 1, p. 2, Dec. 2018.

[11] M. Miola, Y. Pakzad, S. Banijamali, S. Kargozar, C. Vitale-Brovarone, A. Yazdanpanah, O. Bretcanu, A. Ramedani, E. Vernè, and M. Mozafari, "Glass-ceramics for cancer treatment: So close, or yet so far?" *Acta Biomaterialia*, vol. 83, pp. 55–70, Jan. 2019.

[12] J. Peng, J. Zhao, Y. Long, Y. Xie, J. Nie, and L. Chen, "Magnetic materials in promoting bone regeneration," *Frontiers Mater.*, vol. 6, p. 268, Nov. 2019.

[13] Y. Yan, Y. Zhang, Y. Zuo, Q. Zou, J. Li, and Y. Li, "Development of Fe_3O_4–HA/PU superparamagnetic composite porous scaffolds for bone repair application," *Mater. Lett.*, vol. 212, pp. 303–306, Feb. 2018.

[14] Y. Zhao, T. Fan, J. Chen, J. Su, X. Zhi, P. Pan, L. Zou, and Q. Zhang, "Magnetic bioinspired micro/nanostructured composite scaffold for bone regeneration," *Colloids Surf. B, Biointerfaces*, vol. 174, pp. 70–79, Feb. 2019.

[15] V. Goranov, T. Shelyakova, R. De Santis, Y. Haranava, A. Makhaniok, A. Gloria, A. Tampieri, A. Russo, E. Kon, M. Marcacci, L. Ambrosio, and V. A. Dediu, "3D patterning of cells in magnetic scaffolds for tissue engineering," *Sci. Rep.*, vol. 10, no. 1, pp. 1–8, Dec. 2020.

[16] M. Filippi, B. Dasen, J. Guerrero, F. Garello, G. Isu, G. Born, M. Ehrbar, I. Martin, and A. Scherberich, "Magnetic nanocomposite hydrogels and static magnetic field stimulate the osteoblastic and vasculogenic profile of adipose-derived cells," *Biomaterials*, vol. 223, Dec. 2019, Art. no. 119468.

[17] K. M. Sajesh, A. Ashokan, G. S. Gowd, T. B. Sivanarayanan, A. K. K. Unni, S. V. Nair, and M. Koyakutty, "Magnetic 3D scaffold: A theranostic tool for tissue regeneration and non-invasive imaging *in vivo*," *Nanomed., Nanotechnol., Biol. Med.*, vol. 18, pp. 179–188, Jun. 2019.

[18] D. Bian, L. Qin, W. Lin, D. Shen, H. Qi, X. Shi, G. Zhang, H. Liu, H. Yang, J. Wang, D. Zhang, and Y. Zheng, "Magnetic resonance (MR) safety and compatibility of a novel iron bioresorbable scaffold," *Bioactive Mater.*, vol. 5, no. 2, pp. 260–274, Jun. 2020.

[19] A. Luetke, P. A. Meyers, I. Lewis, and H. Juergens, "Osteosarcoma treatment—Where do we stand? A state of the art review," *Cancer Treatment Rev.*, vol. 40, no. 4, pp. 523–532, May 2014.

[20] Y. Yang, L. Han, Z. He, X. Li, S. Yang, Y. Zhang, D. Li, Y. Yang, and Z. Yang, "Advances in limb salvage treatment of osteosarcoma," *J. Bone Oncol.*, vol. 10, pp. 36–40, Mar. 2018.

[21] C. Meazza, S. Bastoni, and P. Scanagatta, "What is the best clinical approach to recurrent/refractory osteosarcoma?" *Cancers*, vol. 11, no. 3, pp. 415–428, 2020.

[22] C. Dahlin, A. Linde, J. Gottlow, and S. Nyman, "Healing of bone defects by guided tissue regeneration," *Plastic Reconstructive Surg.*, vol. 81, no. 5, pp. 672–676, May 1988.

[23] A. Lindahl, M. Brittberg, D. Gibbs, J. I. Dawson, J. Kanczler, C. Black, R. Tare, and R. O. Oreffo, "Cartilage and bone regeneration," in *Tissue Engineering*, C. A. V. Blitterswijk and J. D. Boer, Eds., 2nd ed. Oxford, U.K.: Academic, 2015, ch. 16, pp. 529–582.

[24] H. Ma, T. Li, Z. Huan, M. Zhang, Z. Yang, J. Wang, J. Chang, and C. Wu, "3D printing of high-strength bioscaffolds for the synergistic treatment of bone cancer," *NPG Asia Mater.*, vol. 10, no. 4, pp. 31–44, Apr. 2018.

[25] F. D. Cojocaru, V. Balan, I. M. Popa, A. Munteanu, A. Anghelache, and L. Verestiuc, "Magnetic composite scaffolds for potential applications in radiochemotherapy of malignant bone tumors," *Medicina*, vol. 55, no. 5, p. 153, May 2019.

[26] N. R. Datta, H. P. Kok, H. Crezee, U. S. Gaipl, and S. Bodis, "Integrating loco-regional hyperthermia into the current oncology practice: SWOT and TOWS analyses," *Frontiers Oncol.*, vol. 10, Jun. 2020.

[27] S.-Y. Lee, G. Fiorentini, A. M. Szasz, G. Szigeti, A. Szasz, and C. A. Minnaar, "Quo vadis oncological hyperthermia (2020)?" *Frontiers Oncol.*, vol. 10, p. 1690, Sep. 2020.

[28] S. A. Leon, S. O. Asbell, H. H. Arastu, G. Edelstein, A. J. Packel, S. Sheehan, I. Daskai, G. G. Guttmann, and I. Santos, "Effects of hyperthermia on bone. II. Heating of bone*in vivo*and stimulation of bone growth," *Int. J. Hyperthermia*, vol. 9, no. 1, pp. 77–87, Jan. 1993.

[29] E. Chung and M. N. Rylander, "Response of preosteoblasts to thermal stress conditioning and osteoinductive growth factors," *Cell Stress Chaperones*, vol. 17, no. 2, pp. 203–214, Mar. 2012.

[30] D. Ye, Y. Xu, H. Zhang, T. Fu, L. Jiang, and Y. Bai, "Effects of low-dose microwave on healing of fractures with titanium alloy internal fixation: An experimental study in a rabbit model," *PLoS ONE*, vol. 8, no. 9, Sep. 2013, Art. no. e75756.

[31] K. Ikuta, H. Urakawa, E. Kozawa, S. Hamada, T. Ota, R. Kato, H. Honda, T. Kobayashi, N. Ishiguro, and Y. Nishida, "*In vivo* heat-stimulus-triggered osteogenesis," *Int. J. Hyperthermia*, vol. 31, no. 1, pp. 58–66, Jan. 2015.

[32] E. B. Dolan, M. G. Haugh, M. C. Voisin, D. Tallon, and L. M. McNamara, "Thermally induced osteocyte damage initiates a remodelling signaling cascade," *PLoS ONE*, vol. 10, no. 3, Mar. 2015, Art. no. e0119652.

[33] F. Ghorbani, A. Zamanian, A. Shams, A. Shamoosi, and A. Aidun, "Fabrication and characterisation of super-paramagnetic responsive PLGA–gelatine–magnetite scaffolds with the unidirectional porous structure: A physicochemical, mechanical, and *in vitro* evaluation," *IET Nanobiotechnol.*, vol. 13, no. 8, pp. 860–867, Oct. 2019.

[34] M. M. Fernandes, D. M. Correia, C. Ribeiro, N. Castro, V. Correia, and S. Lanceros-Mendez, "Bioinspired three-dimensional magnetoactive scaffolds for bone tissue engineering," *ACS Appl. Mater. Interfaces*, vol. 11, no. 48, pp. 45265–45275, Dec. 2019.

[35] M. Banobre-Lopez, Y. Pineiro-Redondo, M. Sandri, A. Tampieri, R. De Santis, V. A. Dediu, and J. Rivas, "Hyperthermia induced in magnetic scaffolds for bone tissue engineering," *IEEE Trans. Magn.*, vol. 50, no. 11, pp. 1–7, Dec. 2014.

[36] J. Shi, J. Yang, L. Zhu, L. Li, Z. Li, and X. Wang, "A porous scaffold design method for bone tissue engineering using triply periodic minimal surfaces," *IEEE Access*, vol. 6, pp. 1015–1022, 2018.

[37] A. Syahrom, M. R. A. Kadir, J. Abdullah, and A. Öchsner, "Permeability studies of artificial and natural cancellous bone structures," *Med. Eng. Phys.*, vol. 35, no. 6, pp. 792–799, Jun. 2013.

[38] A. Boccaccio, A. E. Uva, M. Fiorentino, G. Mori, and G. Monno, "Geometry design optimization of functionally graded scaffolds for bone tissue engineering: A mechanobiological approach," *PLoS ONE*, vol. 11, no. 1, Jan. 2016, Art. no. e0146935.

[39] V. J. Challis, A. P. Roberts, J. F. Grotowski, L.-C. Zhang, and T. B. Sercombe, "Prototypes for bone implant scaffolds designed via topology optimization and manufactured by solid freeform fabrication," *Adv. Eng. Mater.*, vol. 12, no. 11, pp. 1106–1110, Nov. 2010.

[40] H. A. Almeida and P. J. Bártolo, "Design of tissue engineering scaffolds based on hyperbolic surfaces: Structural numerical evaluation," *Med. Eng. Phys.*, vol. 36, no. 8, pp. 1033–1040, Aug. 2014.

[41] J. E. Schroeder and R. Mosheiff, "Tissue engineering approaches for bone repair: Concepts and evidence," *Injury*, vol. 42, no. 6, pp. 609–613, Jun. 2011.

[42] D.-J. Yoo, "Computer-aided porous scaffold design for tissue engineering using triply periodic minimal surfaces," *Int. J. Precis. Eng. Manuf.*, vol. 12, no. 1, pp. 61–71, Feb. 2011.

[43] H.-Y. Xu and N. Gu, "Magnetic responsive scaffolds and magnetic fields in bone repair and regeneration," *Frontiers Mater. Sci.*, vol. 8, no. 1, pp. 20–31, Mar. 2014.

[44] P. J. F. Gandy, D. Cvijović, A. L. Mackay, and J. Klinowski, "Exact computation of the triply periodic d ('diamond') minimal surface," *Chem. Phys. Lett.*, vol. 314, nos. 5–6, pp. 543–551, Dec. 1999.

[45] P. J. F. Gandy and J. Klinowski, "Exact computation of the triply periodic schwarz p minimal surface," *Chem. Phys. Lett.*, vol. 322, no. 6, pp. 579–586, Jun. 2000.

[46] P. J. F. Gandy and J. Klinowski, "Exact computation of the triply periodic g ('gyroid') minimal surface," *Chem. Phys. Lett.*, vol. 321, nos. 5–6, pp. 363–371, May 2000.

[47] R. Goldman, "Curvature formulas for implicit curves and surfaces," *Comput. Aided Geometric Des.*, vol. 22, no. 7, pp. 632–658, 2005.

[48] J. C. Dinis, T. F. Morais, P. H. J. Amorim, R. B. Ruben, H. A. Almeida, P. N. Inforçati, P. J. Bártolo, and J. V. L. Silva, "Open source software for the automatic design of scaffold structures for tissue engineering applications," *Proc. Technol.*, vol. 16, pp. 1542–1547, Jan. 2014.

[49] Z. Xu, Q. Wang, and J. Li, "Modeling porous structures with fractal rough topography based on triply periodic minimal surface for additive manufacturing," *Rapid Prototyping J.*, vol. 23, no. 2, pp. 257–272, Mar. 2017.

[50] J. Feng, J. Fu, C. Shang, Z. Lin, and B. Li, "Porous scaffold design by solid T-splines and triply periodic minimal surfaces," *Comput. Methods Appl. Mech. Eng.*, vol. 336, pp. 333–352, Jul. 2018.

[51] E. Abbena, S. Salamon, and A. Gray, *Modern Differential Geometry of Curves and Surfaces With Mathematica*. Boca Raton, FL, USA: CRC Press, 2017.

[52] MATLAB Central File Exchange, Sven. *Stlwrite—Write ASCII or Binary STL Files*. Accessed: May 19, 2021. [Online]. Available: https://www.mathworks.com/matlabcentral/fileexchange/20922-stlwrite-write-ascii-or-binary-stl-files
[53] ProtoPasta. *Iron PLA*. Accessed: Dec. 20, 2021. [Online]. Available: https://www.proto-pasta.com/products/magnetic-iron-pla
[54] L. M. Bollig, M. V. Patton, G. S. Mowry, and B. B. Nelson-Cheeseman, "Effects of 3-D printed structural characteristics on magnetic properties," *IEEE Trans. Magn.*, vol. 53, no. 11, pp. 1–6, Nov. 2017.
[55] J. Laureto, J. Tomasi, J. A. King, and J. M. Pearce, "Thermal properties of 3-D printed polylactic acid-metal composites," *Prog. Additive Manuf.*, vol. 2, nos. 1–2, pp. 57–71, Jun. 2017.
[56] O. Zmeskal, L. Marackova, T. Lapcikova, P. Mencik, and R. Prikryl, "Thermal properties of samples prepared from polylactic acid by 3D printing," in *Proc. AIP Conf. Proc.*, vol. 2305, no. 1, 2020, Art. no. 020022.
[57] K. Lai, W. Jiang, J. Z. Tang, Y. Wu, B. He, G. Wang, and Z. Gu, "Superparamagnetic nano-composite scaffolds for promoting bone cell proliferation and defect reparation without a magnetic field," *RSC Adv.*, vol. 2, no. 33, p. 13007, 2012.
[58] H. Hu, W. Jiang, F. Lan, X. Zeng, S. Ma, Y. Wu, and Z. Gu, "Synergic effect of magnetic nanoparticles on the electrospun aligned superparamagnetic nanofibers as a potential tissue engineering scaffold," *RSC Adv.*, vol. 3, no. 3, pp. 879–886, 2013.
[59] J.-J. Kim, R. K. Singh, S.-J. Seo, T.-H. Kim, J.-H. Kim, E.-J. Lee, and H.-W. Kim, "Magnetic scaffolds of polycaprolactone with functionalized magnetite nanoparticles: Physicochemical, mechanical, and biological properties effective for bone regeneration," *RSC Adv.*, vol. 4, no. 33, pp. 17325–17336, 2014.
[60] *Standard Test Method for Determining Specific Heat Capacity by Differential Scanning Calorimetry*, Standard ASTM E1269-11(2018), ASTM International, West Conshohocken, PA, USA, 2018. [Online]. Available: http://www.astm.org
[61] A. Makridis, S. Curto, G. C. van Rhoon, T. Samaras, and M. Angelakeris, "A standardisation protocol for accurate evaluation of specific loss power in magnetic hyperthermia," *J. Phys. D, Appl. Phys.*, vol. 52, no. 25, Jun. 2019, Art. no. 255001.
[62] I. Rubia-Rodríguez *et al.*, "Whither magnetic hyperthermia? A tentative roadmap," *Materials*, vol. 14, no. 4, p. 706, Feb. 2021.
[63] J. Wells, D. Ortega, U. Steinhoff, S. Dutz, E. Garaio, O. Sandre, E. Natividad, M. M. Cruz, F. Brero, P. Southern, Q. A. Pankhurst, and S. Spassov, "Challenges and recommendations for magnetic hyperthermia characterization measurements," *Int. J. Hyperthermia*, vol. 38, no. 1, pp. 447–460, Jan. 2021.
[64] H. D. Trefná, M. Schmidt, G. C. van Rhoon, H. P. Kok, S. S. Gordeyev, U. Lamprecht, D. Marder, J. Nadobny, P. Ghadjar, S. Abdel-Rahman, A. M. Kukiełka, V. Strnad, M. D. Hurwitz, Z. Vujaskovic, C. J. Diederich, P. R. Stauffer, and J. Crezee, "Quality assurance guidelines for interstitial hyperthermia," *Int. J. Hyperthermia*, vol. 36, no. 1, pp. 276–293, Jan. 2019.
[65] I. Andreu and E. Natividad, "Accuracy of available methods for quantifying the heat power generation of nanoparticles for magnetic hyperthermia," *Int. J. Hyperthermia*, vol. 29, no. 8, pp. 739–751, Dec. 2013.
[66] A. Fanti, M. B. Lodi, G. Vacca, and G. Mazzarella, "Numerical investigation of bone tumor hyperthermia treatment using magnetic scaffolds," *IEEE J. Electromagn., RF Microw. Med. Biol.*, vol. 2, no. 4, pp. 294–301, Dec. 2018.
[67] M. B. Lodi, A. Fanti, G. Muntoni, and G. Mazzarella, "A multiphysic model for the hyperthermia treatment of residual osteosarcoma cells in upper limbs using magnetic scaffolds," *IEEE J. Multiscale Multiphys. Comput. Techn.*, vol. 4, pp. 337–347, 2019.
[68] H. Kato, K. Yoshimura, M. Kuroda, A. Yoshida, K. Hanamoto, S. Kawasaki, K. Shibuya, Y. Yamamoto, M. Tsunoda, M. Takemoto, and Y. Hiraki, "Development of a phantom compatible for MRI and hyperthermia using carrageenan gel—Relationship between dielectric properties and NaCl concentration," *Int. J. Hyperthermia*, vol. 20, no. 5, pp. 529–538, 2004.
[69] R. A. O. Jaime, R. L. Q. Basto, B. Lamien, H. R. B. Orlande, S. Eibner, and O. Fudym, "Fabrication methods of phantoms simulating optical and thermal properties," *Proc. Eng.*, vol. 59, pp. 30–36, Jan. 2013.
[70] C. Dichtl, P. Sippel, and S. Krohns, "Dielectric properties of 3D printed polylactic acid," *Adv. Mater. Sci. Eng.*, vol. 2017, pp. 1–10, Jul. 2017.
[71] E. Natividad, M. Castro, and A. Mediano, "Adiabatic vs. non-adiabatic determination of specific absorption rate of ferrofluids," *J. Magn. Magn. Mater.*, vol. 321, no. 10, pp. 1497–1500, 2009.
[72] S. K. Kandala, A. Sharma, S. Mirpour, E. Liapi, R. Ivkov, and A. Attaluri, "Validation of a coupled electromagnetic and thermal model for estimating temperatures during magnetic nanoparticle hyperthermia," *Int. J. Hyperthermia*, vol. 38, no. 1, pp. 611–622, Jan. 2021.
[73] I. Antoniac, D. Popescu, A. Zapciu, A. Antoniac, F. Miculescu, and H. Moldovan, "Magnesium filled polylactic acid (PLA) material for filament based 3D printing," *Materials*, vol. 12, no. 5, p. 719, Mar. 2019.
[74] Y. Jiang, J. Ou, Z. Zhang, and Q.-H. Qin, "Preparation of magnetic and bioactive calcium zinc iron silicon oxide composite for hyperthermia treatment of bone cancer and repair of bone defects," *J. Mater. Sci., Mater. Med.*, vol. 22, no. 3, pp. 721–729, Mar. 2011.
[75] J. Zhang, S. Zhao, M. Zhu, Y. Zhu, Y. Zhang, Z. Liu, and C. Zhang, "3D-printed magnetic Fe_3O_4/MBG/PCL composite scaffolds with multifunctionality of bone regeneration, local anticancer drug delivery and hyperthermia," *J. Mater. Chem. B*, vol. 2, no. 43, pp. 7583–7595, 2014.
[76] M. B. Lodi, N. Curreli, S. Zappia, L. Pilia, M. F. Casula, S. Fiorito, I. Catapano, F. Desogus, T. Pellegrino, I. Kriegel, L. Crocco, G. Mazzarella, and A. Fanti, "Influence of magnetic scaffold loading patterns on their hyperthermic potential against bone tumors," *IEEE Trans. Biomed. Eng.*, early access, Dec. 9, 2021, doi: 10.1109/TBME.2021.3134208.
[77] M. B. Lodi, A. Fanti, A. Vargiu, M. Bozzi, and G. Mazzarella, "A multiphysics model for bone repair using magnetic scaffolds for targeted drug delivery," *IEEE J. Multiscale Multiphys. Comput. Techn.*, vol. 6, pp. 201–213, 2021, doi: 10.1109/JMMCT.2021.3134786.

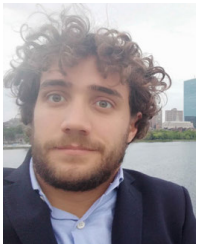

MATTEO BRUNO LODI (Student Member, IEEE) received the bachelor's degree in biomedical engineering from the University of Cagliari, Cagliari, in 2016, and the master's degree in biomedical engineering from the Politecnico di Torino, Turin, Italy, in 2018. He is currently pursuing the Ph.D. degree in electronic engineering and computer science with the University of Cagliari. His research activity deals with the modeling of bioelectromagnetic phenomena, especially hyperthermia treatment; the study, manufacturing, and synthesis of magnetic biomaterials for tissue engineering applications; and the use of microwave for biotechnology and environmental applications. He is a member of the Editorial Board of the IEEE Future Directions Technology Policy and Ethics newsletter. He was awarded as the Young Scientists at the General Assembly and Scientific Symposium of URSI 2020 and 2021. He has been appointed as a Representative for the Young Professionals of IEEE Region 8 Nanotechnology Council.

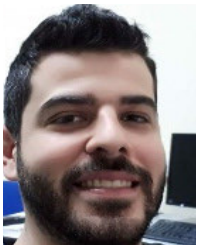

ANTONIS MAKRIDIS is currently a Postdoctoral Researcher. Being a member of MagnaCharta Group (magnacharta.physics.auth.gr), since 2010, resulted to his active participation to several projects related to magnetic nanomaterials and to his Ph.D. thesis defense with title Magnetic Nanostructures and Nanomagnetism for Modern Biomedical Applications (defended on April 2019). As a Material Science and Physics Researcher, he worked in the synthesis of iron-based magnetic nanostructures and he has studied their use as agents in biological applications. His research interests include chemical synthesis and characterization of diverse types of nanoparticles, either destined for specific applications or from sheer scientific curiosity. Additionally, he is an expert on standardizing and setting novel experimental protocols on modern nanoparticle applications. Since 2009, he has been a Reviewer in 19 international scientific journals and he has published 20 manuscripts in peer-reviewed journals.

NICOLA M. CARBONI received the bachelor's degree in mathematics from the University of Cagliari, in 2019. He is currently involved in the topological modeling for material science and biomedical applications, while working on differential problems.

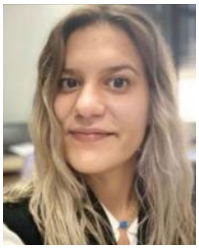

KONSTANTINA KAZELI graduated from the Physics Department, University of Ioannina. She received the master's degree in biomedical and molecular science in diagnosing and treating diseases from the Medical Department, Democritus University of Thrace, with a thesis title "Antibacterial and Oxidative Stress Study of Bioceramic Nanoparticles for Bone Regeneration Synthesis and Characterization." She is currently pursuing the Ph.D. degree. She is a member of MagnaCharta Group (magnacharta.physics.auth.gr), since 2020, as a Ph.D. candidate and a Researcher with a dissertation title "Synthesis and Characterization of Nanomagnetic Bioceramics for Biomedical Applications." Her research interests include synthesis of innovative magnetic-bioceramic nanoparticles, in order to achieve the best possible biological efficiency and to expand the huge potential of multifunctional nanocomposites and scaffolds in the field of nanomedicine as multifunctional biomedical agents combining diverse therapeutic results in tumor treatments, bone regeneration, magnetic hyperthermia, and drug delivery.

NICOLA CURRELI received the M.Sc. degree from the University of Genoa, Genoa, Italy, in 2016, and the Ph.D. degree in electronic engineering from the University of Cagliari, Cagliari, Italy, and the Italian Institute of Technology (IIT), Genoa, Italy, in 2020. In 2019, he was a Visiting Researcher with the Physics and Mechanical Engineering Departments, Columbia University, City of New York, NY, USA. After the Ph.D., he held a fellow position at the Graphene Labs, IIT, within the WP12 (Energy storage) of the Graphene Core 2 Project - Graphene Flagship. He is currently a Postdoctoral Researcher at the Functional Nanosystems Group, IIT. His research activity is focused on the study of low-dimensional materials and their application in the fields of electronics and photonics.

THEODOROS SAMARAS (Member, IEEE) received the M.Sc. degree (Hons.) in medical physics from the University of Surrey, U.K., and the Ph.D. degree from the Aristotle University of Thessaloniki, Greece. He subsequently joined the Swiss Federal Institute of Technology (ETH), Zürich, where he was involved in the computational dosimetry of electromagnetic fields. He later moved to the Erasmus Medical Centre of Rotterdam, where he worked on the quality assurance of superficial microwave hyperthermia with a Marie-Curie Postdoctoral Fellowship from the European Commission. In December 1999, he returned to the Aristotle University of Thessaloniki, where he is currently a Professor of bioelectromagnetics. His research interests include numerical techniques and computational multiphysics modeling with applications in biomedical technology and the safety of electromagnetic fields.

MAKIS ANGELAKERIS received the Ph.D. degree in magnetic nanostructures from the Aristotle University of Thessaloniki, in 2000. Since 2000, he has been involved in biomedical applicability schemes of magnetic nanostructures, such as magnetic particle hyperthermia and magnetomechanical actuation. He is currently a Professor with the School of Physics, Aristotle University of Thessaloniki. He is the Group Leader of MagnaCharta Group (http://magnacharta.physics.auth.gr). He has published 133 manuscripts in peer-reviewed journals and received 3395 citations by 2424 document (Scopus 12/2021). His research interests include magnetic nanostructures initiating from synthesis of magnetic multilayers and magnetic nanoparticles and corresponding magnetic characterizations, including static and dynamic magnetic measurements.

GIUSEPPE MAZZARELLA (Senior Member, IEEE) graduated *(summa cum laude)* in electronic engineering from the Università Federico II of Naples, in 1984. He received the Ph.D. degree in electronic engineering and computer science, in 1989. In 1990, he became an Assistant Professor at the Dipartimento di Ingegneria Elettronica, Università Federico II of Naples. Since 1992, he has been with the Dipartimento di Ingegneria Elettrica ed Elettronica, Università di Cagliari, first as an Associate Professor and then, since 2000, as a Full Professor, teaching courses in electromagnetics, microwave, antennas and remote sensing. He is the author (or coauthor) of over 70 articles in international journals, and is a reviewer for many EM journals. His research activity has focused mainly on: efficient design of large arrays of slots, power synthesis of array factor, with emphasis on inclusion of constraints, microwave holography techniques for the diagnosis of large reflector antennas, and use of evolutionary programming for the solution of inverse problems, in particular problems of synthesis of antennas and periodic structures.

ALESSANDRO FANTI (Member, IEEE) received the Laurea degree in electronic engineering and the Ph.D. degree in electronic engineering and computer science from the University of Cagliari, Cagliari, Italy, in 2006 and 2012, respectively. He worked as a Postdoctoral Fellow with the Electromagnetic Group, University of Cagliari, from 2013 to 2016, where he is currently an Assistant Professor. From 2020 to 2023, he acts as a Principal Investigator of the "IAPC" Project, funded with €5 million by the Italian Ministry of Economic Development (MISE), within the AGRIFOOD PON I&C 2014–2020 (CUP: B21B1900064008 COR: 1406652). His research activity involves the use of numerical techniques for modes computation of guiding structures, optimization techniques, analysis and design of waveguide slot arrays, analysis and design of patch antennas, radio propagation in urban environment, modeling of bio-electromagnetic phenomena, microwave exposure systems for biotechnology and bio-agriculture. He is an Associate Editor of the IEEE JOURNAL OF ELECTROMAGNETICS, RF-AND MICROWAVES IN MEDICINE AND BIOLOGY (J-ERM).